Journal of the Mechanics and Physics of Solids 81 (2015) 75–90

Contents lists available at ScienceDirect

Journal of the Mechanics and Physics of Solids

journal homepage: www.elsevier.com/locate/jmps

Crack instability of ferroelectric solids under alternative electric loading

Chen Hao-Sen[a], Wang He-Ling[a], Pei Yong-Mao[b], Wei Yu-Jie[c], Liu Bin[a,*], Fang Dai-Ning[b,**]

[a] Department of Engineering Mechanics, Tsinghua University, Beijing 100084, PR China
[b] LTCS and College of Engineering, Peking University, Beijing 100871, PR China
[c] LNM, Institute of Mechanics, Chinese Academy of Sciences, Beijing 100190, PR China

ARTICLE INFO

Article history:
Received 23 September 2014
Received in revised form
23 April 2015
Accepted 24 April 2015
Available online 12 May 2015

Keywords:
Electro-thermal-mechanical coupling
Crack instability
Ferroelectric materials
Safe operating area

ABSTRACT

The low fracture toughness of the widely used piezoelectric and ferroelectric materials in technological applications raises a big concern about their durability and safety. Up to now, the mechanisms of electric-field induced fatigue crack growth in those materials are not fully understood. Here we report experimental observations that alternative electric loading at high frequency or large amplitude gives rise to dramatic temperature rise at the crack tip of a ferroelectric solid. The temperature rise subsequently lowers the energy barrier of materials for domain switch in the vicinity of the crack tip, increases the stress intensity factor and leads to unstable crack propagation finally. In contrast, at low frequency or small amplitude, crack tip temperature increases mildly and saturates quickly, no crack growth is observed. Together with our theoretical analysis on the non-linear heat transfer at the crack tip, we constructed a safe operating area curve with respect to the frequency and amplitude of the electric field, and validated the safety map by experiments. The revealed mechanisms about how electro-thermal-mechanical coupling influences fracture can be directly used to guide the design and safety assessment of piezoelectric and ferroelectric devices.

1. Introduction

Ferroelectric materials have been widely employed in sensors, transducers, actuators and ferroelectric memories (Eerenstein et al., 2006; Haertling, 1999; Scott, 2007) for their excellent piezoelectric property and intrinsic switchable spontaneous polarization. Depending on the application, the ferroelectric devices are always exposed to cyclic electric loading (Kuna, 2010). However, the low fracture toughness of ferroelectric materials makes it hard to resist the growth and coalescence of unavoidable initial cracks under alternative electric loading.

These cyclic electric loading induced crack propagation phenomenon was first observed by Cao and Evans (1994) and confirmed by Lynch et al. (1995). During the last decade, both the experimental and theoretical studies concerning the alternative electric load induced crack growth have been performed by several research groups, such as Lynch et al. (1995a, 1995b), Zhu and Yang (1998), Weitzing et al. (1999), Liu et al. (2002), Fang et al. (2004, 2005, 2007, 2008, 2011), Jeong and

* Corresponding author. Fax: +86 10 62786194.
** Corresponding author. Fax: +86 10 62781824.
E-mail addresses: liubin@tsinghua.edu.cn (B. Liu), fangdn@pku.edu.cn (D.-N. Fang).

http://dx.doi.org/10.1016/j.jmps.2015.04.014
0022-5096/

Beom (2004), Beom and Jeong (2005), Westram et al. (2007a, 2007b, 2009), Gehrig et al. (2008), Abdollahi and Arias (2012, 2013, 2014), Zhang et al. (2013), Jiang et al. (2014). Most of the published works concerned the insulating crack propagating in the direction perpendicular to the electric field under alternative electric loading with different field strength and frequency. It was widely accepted that there exists both electric field amplitude threshold and frequency threshold for the crack growth: (1) Amplitude threshold E_{th}. The field strength typically needs to exceed a certain level before crack propagation starts. Cao and Evans (1994) observed that the cyclic electric induced crack propagates for applied amplitudes $E \geq 1.1\ E_c$ (coercive field), while Zhu and Yang (1998) concluded that the certain level can be below the E_c based on the experimental tests of PZT-5 material. Fang et al. (2004) observed that the electric amplitude threshold E_{th} equals to 0.797 E_c. (2) Frequency threshold f_{th}. Fang and Liu (2013) also found that the crack growth is frequency-dependent, as was observed by Weitzing et al. (1999). They reported that until the applied frequency is lower than the threshold value $f_{th}=341.53$ Hz, obvious fatigue crack propagation can be observed. Up to now, it is difficult to grasp the phenomena in a theoretical manner for the variety of experimental conditions and results, and the mechanisms of electric-field induced fatigue crack growth are still not fully understood.

Furthermore, the thermal effect to fracture has been largely neglected since most piezoelectric or ferroelectric samples were immersed in oil during experiments to prevent possible electrical breakdown. In practices, however, most of the piezoelectric or ferroelectric devices are exposed to air. Given the thermal conductivity of ferroelectrics-air is one to two orders of magnitude smaller than that of ferroelectrics-oil, current experiments with ferroelectric samples immersed in oil differ significantly from their serving environment. Thermal effect could affect the piezoelectric behavior or even destroy the devices and their ancillary components, such as soldered connections and adhesively bonded joints (Härdtl, 1982; Jiehui et al., 1996; Lynch et al., 1995; Stewart and Cain, 2014; Uchino, 1998). This inconsistence would have great influence on the fracture mechanics of ferroelectric materials. More important, a connection between the electro-thermal-mechanical coupling at a crack tip (Livne et al., 2010) and the failure behaviors of the devices remains rarely explored, to our best knowledge.

In this paper, the mechanisms of self-heating induced crack instability of ferroelectric materials are researched systematically. We present experimental observations on how alternative electric loading at different frequency or amplitude would give rise to distinct temperature field at the crack tip and crack stability in Section 2. Further theoretical analysis and finite element analysis on the non-linear heat transfer problem at the crack tip shown in Section 3 sheds light on how electro-thermal-mechanical coupling influences fracture, which enables us to construct a fracture phase map for the design and safety assessment of piezoelectric and ferroelectric devices. We conclude in Section 4.

2. Experimental procedure

2.1. Materials and specimens

The material used for the experiment was the commercial PZT-5 ($Pb[Zr,Ti]O_3$) ceramic with Zr:Ti=0.52:0.48 manufactured by Hongsen Electronic Materials Co. Ltd., China. It has a tetragonal crystal structure at room temperature and an average rain size of 3 μm. The soft ferroelectric ceramics had a Curie temperature above $\theta_c=320$ °C. The coercive electric field E_c is temperature-dependent and frequency-dependent. It equals to be about 0.8 kV/mm at the fixed frequency $f=1$ Hz and temperature $\theta=20$ °C, which is defined as $E_{c0}=E_c$ ($f=1$ Hz, $\theta=20$ °C). The saturation polarization P_s is also temperature and frequency dependent, it equals to be about 40.0 μC/cm^2 at the fixed frequency $f=1$ Hz and temperature $\theta=20$ °C. Therefore we have $P_0=P_s$ ($f=1$ Hz, $\theta=20$ °C). Rectangular samples with a central crack were used, as shown in Fig. 1.

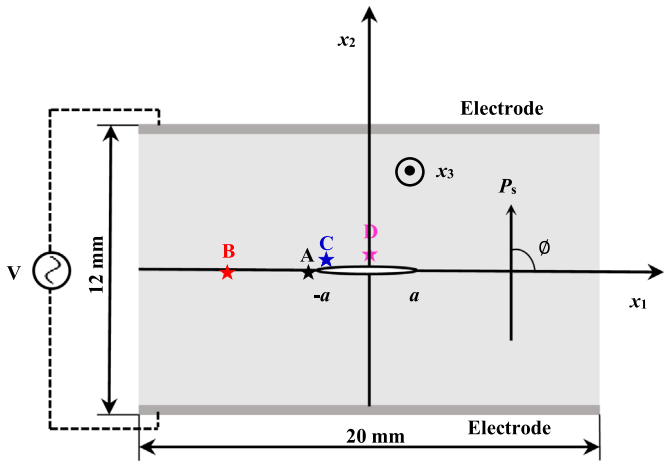

Fig. 1. Schematic illustration of a central crack in ferroelectric solids.

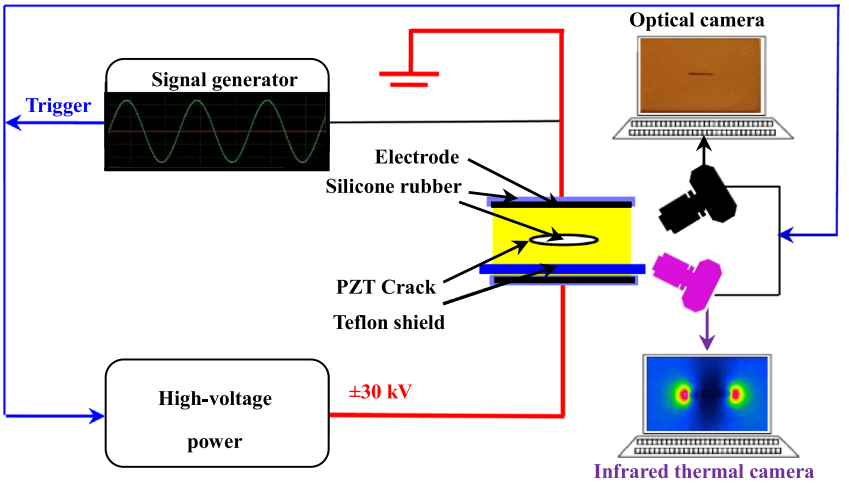

Fig. 2. Schematic of the *in-situ* experimental setup.

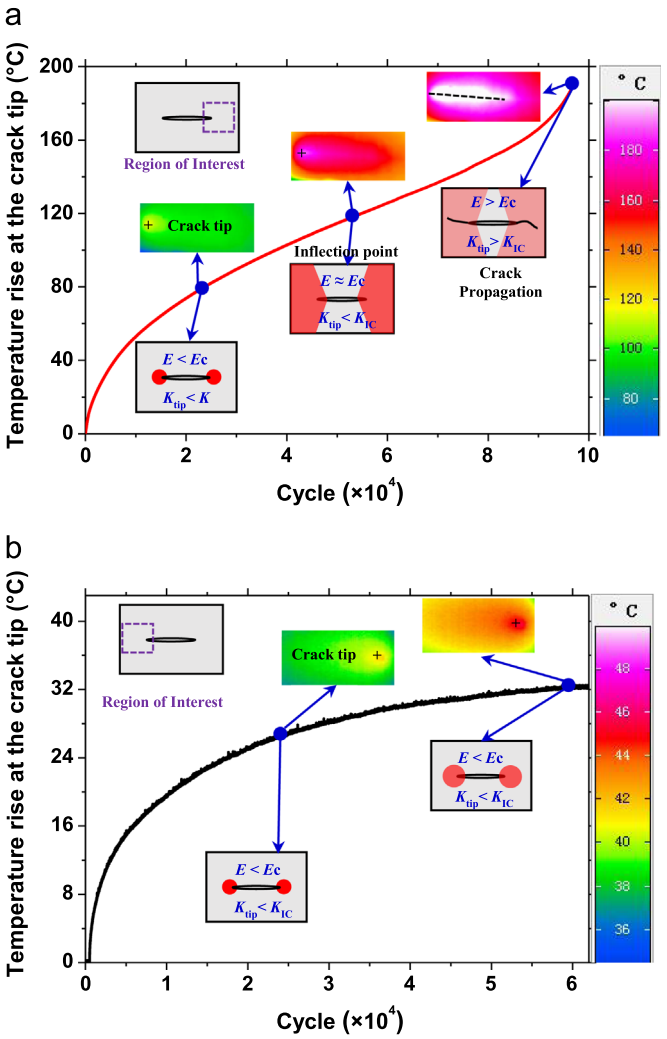

Fig. 3. Temperature rise and infrared thermal images with cycles. (a) Significant and continuous temperature rise and resultant crack instability at high frequency $f=1$ *k*Hz ($E=0.75\ E_{c0}$), see Supplementary Movie 1 and 2. (b) Saturating temperature with stable crack at low conditions $f=100$ Hz ($E=0.75\ E_{c0}$), see Supplementary Movie 4 and 5.

Supplementary material related to this article can be found online at doi:10.1016/j.jmps.2015.04.014.

The sample size is $20 \times 12 \times 3$ mm along x_1-axis, x_2-axis, and the thickness direction x_3-axis. The poling and electric loading directions both are parallel to the x_2-axis. A central crack of 3 mm in length was manufactured by using the ultrasonic pulse technique with a 0.1 mm-thick moving diamond blade. By using boron carbide and at high frequency of about 20–23 kHz, lapping grains can make a crack with a width of less than 100–200 μm. The process has been described in detail in our early work (Soh et al., 2003), therefore, it will not be reiterated here. A soft insulated silicone was filled into the crack and cued completely in an oven at 50 °C, which was used to represent the impermeable electric boundary condition.

2.2. Experimental setups

Previous work has demonstrated that heat generation in the ferroelectric bulk without pre-cracks occurs as soon as reversal polarization finishes (Chen et al., 2013). By noting that the electric loading induced reverse domain switching zone is identical to that of the heat generation zone, we develop a noncontact infrared inspection method to determine the domain switching zone *via in situ* observing the heat generation zone.

The *in-situ* experimental setup was developed based on that reported in our early work (Chen et al., 2013). It consisted of four parts, as shown in Fig. 2: (1) Non-contact temperature measurement system. Infrared thermal camera: VarioCAM hr Research 780, Infratec, Germany; Thermal resolution: 25 mK; Spatial resolution: 0.03 mm; Sampling frequency: 50 Hz. (2) Crack propagation recording system. The self-heating induced crack growth was observed using an optical high-speed microscope (KEYENCE VW-9000, Japan) with 1000 frames per second; (3) High-voltage power supplier system. Signal generator: Agilent 33220A; High-voltage power amplifier: $\pm$ 30 kV Trek Model 20/30C. (4) Insulating system. The electrode surfaces of specimens were covered with silicone rubber to prevent arcing by cutting the discharge paths, while the other parts of the sample were exposed to the air directly.

2.3. Experimental results and discussions

Firstly, we examine the correlation between temperature rise and crack propagation in lead zirconium titanate (PZT) bulk specimen with a central crack, as shown in Fig. 1. The setup allows the samples to be exposed directly to air instead of being immersed in oil. 12 samples under different combinations of the magnitude and frequency were tested.

Fig. 3 presents temperature rise versus cycles during the samples were loaded by alternative electric field with constant amplitude of $E=0.75\ E_{c0}$ and varying frequency. Significant and continuous temperature rise and resultant crack instability at high frequency $f=1$ kHz is observed (see Fig. 3a). The whole temperature curve resembles a "reverse *S*" shape with the reverse inflection point occurs after 5.3×10^4 cycles. After that temperature increases rapidly and can reach as high as 220 °C. In the insets, we show infrared thermal images at different stages, and corresponding videos are supplied in Supplementary Movie 1 and 2. The temperature profile shows three distinct stages: (1) *Stage I*: Before the reverse inflection point, temperature rise around the crack tip is higher than that away from the crack tip. The magnitude of the applied

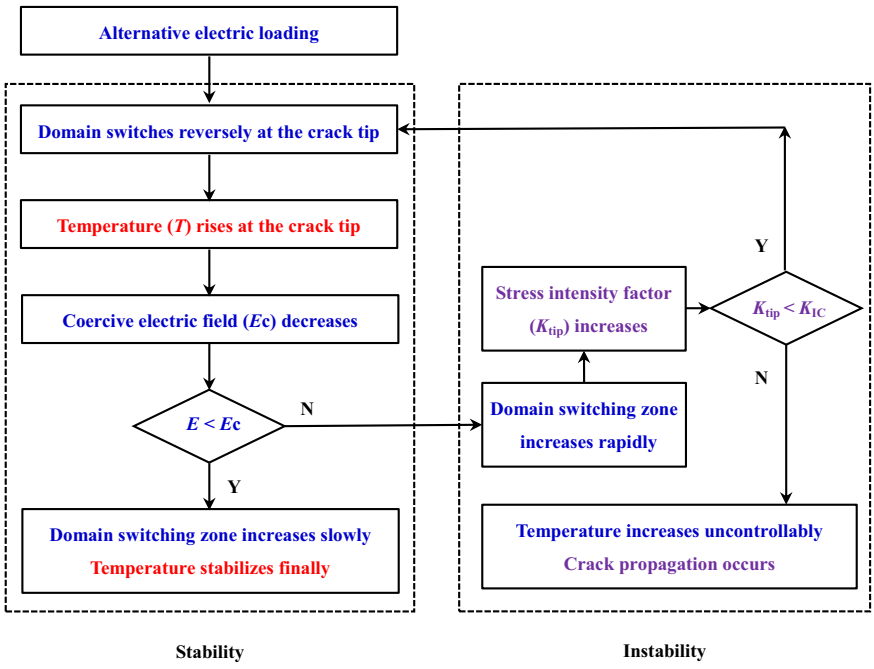

Fig. 4. Flow chart to illustrate the coupled electro-thermal-mechanical nonlinear problem.

electric loading is smaller than the coercive electric field, and heat generates only in the vicinity of the crack tip and transfers to the whole sample. (2) *Stage II*: After the reverse inflection point and before crack propagation, now the magnitude of the applied electric loading is approaching or exceeding the coercive electric field. The domain switching occurs in the most part of the whole bulk except the zone right behind the crack tip. Heat transfers from the domain switching zone (including the crack tip) to the no-domain switching zone (behind the crack tip). And (3) *stage III*: After the initiation of the crack, temperature at the newly formed crack tip increases more dramatically with crack propagation. This positive feedback results in sudden crack running through the whole specimen. The experimental results were different from the conclusion about thresholds for the alternative electric field induced crack propagation in ferroelectric ceramics (Cao and Evans, 1994; Zhu and Yang, 1998; Weitzing et al., 1999; Fang et al., 2004; Fang and Liu, 2013). The loading amplitude and frequency were both beyond the thresholds ($E=0.75\ E_{c0} < E_{th}=0.797\ E_c$, $f=1\ k\,\mathrm{Hz} > f_{th}=341.53\ \mathrm{Hz}$). Furthermore, we normally do not see any forerunner of such electro-thermal-mechanical coupling fracture, which is very dangerous to the safety of ferroelectric devices.

On the contrary, when the samples are under cyclic alternative electric loading at low frequency (100 Hz) and the same amplitude ($E=0.75E_{c0}$), temperature quickly reaches a stable state and no crack growth is observed, as shown in Fig. 3b.

Fig. 4 summaries the experimental observation. If the frequency and the amplitude of the electric loading is high enough, corresponding to the case shown in Fig. 3a, heat transfers from the crack tip to the whole sample. The temperature increases rapidly followed by the decreasing of coercive electric field, which leads to quick increasing of stress intensity factor K_{tip} (T). Crack propagation finally occurs when the stress intensity factor K_{tip} reaches the fracture toughness K_{IC}. When the frequency and the amplitude of the electric loading is low, such as the case shown in Fig. 3b, this kind of mutual interaction effect has less influence than the effect of the heat convection with the surroundings. The temperature finally becomes balanced at the crack tip.

In addition to be sensitive to both frequency and amplitude, the temperature field in the front of a crack tip is also influenced by the waveform of the electric loading. We show in Fig. 5, the temperature evolution at point A under electric loading with three different driving waveforms: unipolar up-triangle, down-triangle and bipolar. The temperature snapshot is obtained right after 100 cycles of electric loading with $E=0.75E_{c0}$ and $f=1$ kHz. Under unipolar up-triangle or down-triangle waveform, the temperature at the crack tip remained nearly unchanged. However, an abrupt temperature increase is observed and the maximum temperature rise reaches 6.17 °C under bipolar electric field. It suggests that domain around the crack tip does not switch repeatedly under unipolar electric field, but switches when the bipolar electric loading is applied. Therefore, we suggest that the bipolar loading should be chosen only as the last option for the devices in service.

Previously, we have shown that the temperature and frequency dependent coercive electric field plays an important role in electro-thermal-mechanical coupling fracture problem. Now we aim to measure the shape and size of the domain switching zone at the crack tip during electric loading. This information is crucial for the fundamental understanding of ferroelectric fracture problems like the mechanism of fatigue crack growth under electric loading.

Fig. 6 presents temperature evolution process near and away at different points, A ($x_1=1.6$ mm, $x_2=0$ mm), B ($x_1=-4.5$ mm, $x_2=0$ mm), C ($x_1=-1.5$ mm, $x_2=0.1$ mm) and D ($x_1=0$ mm, $x_2=0.2$ mm). The 10 cyclic alternative electric loading is applied with the amplitude $E=1E_{c0}$ and the frequency $f=1$ Hz. We see that there are two temperature peak in one cycle at point A, B and C, while no clear temperature peak is observed at point D. Using the *in-situ* experimental setup, our early work (Chen et al., 2013) measured both the temperature rise and strain change of ferroelectric bulk samples in free air under bipolar electric loadings. It was shown that temperature change occurs twice as soon as polarization reversal finishes

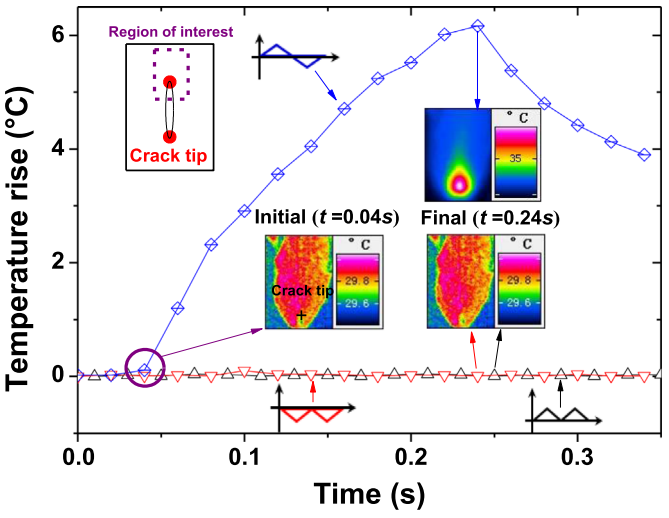

Fig. 5. Temperature rise at the crack tip under different electric waveform (Loading conditions: 1 kHz, 0.75 E_{c0}, 100 cycles): triangle, up-triangle and down-triangle.

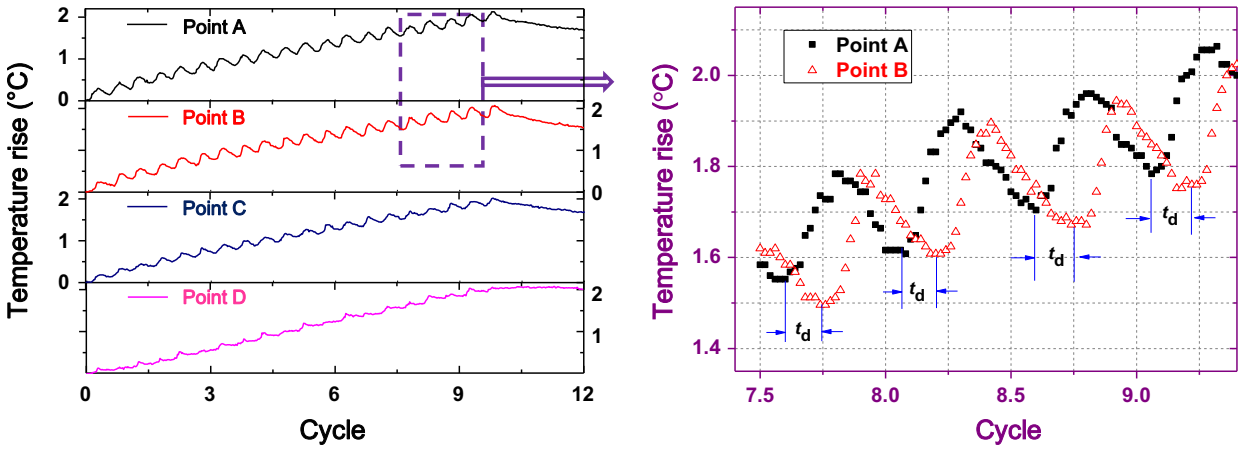

Fig. 6. Temperature rise at different points under loading $E=1E_{c0}$ and $f=1$ *Hz*.

in each cycle of electric loading, and the temperature rise is on the order of 0.2 °C with a complete domain switching. These results suggest that heat generation is mainly caused by the domain switching. As shown in Fig. 6, there are two temperature rise peaks in each cycle at the crack tip of ferroelectric sample and the temperature change is about 0.2 °C, which has been proved to be the result of the reverse domain switching (Chen et al., 2013). Furthermore, we find that temperature rise at point *B* lags obviously behind that at point *A*. It hence suggests that the reverse 180° domain switching near the crack tip happens earlier than that some distance away from the crack tip. By averaging the experimental data of 10 cycles, we obtain the delay time t_d about 0.14 cycle. It means that the electric field intensity factor is about 2.3 at point *A*, which is smaller than the theoretical prediction of 2.9 when using Eq. (10). The difference may originate from the factor that that the real crack tip has a finite radius, which reduces the level of electric field concentration at the crack tip.

3. Electro-thermal-mechanical coupled modeling

3.1. Field coupling equations

During one cycle of bipolar electrical loading, reverse domain switching occurs near the crack tip and most of the energy is dissipated via heat generation. The dissipated energy in the reverse zone generates a temperature field which is determined by the intensity of the heat source and the thermal boundary conditions. The dissipated energy is assumed to be proportional to the electric loading frequency *f* and the volume of the reverse domain switching zone (Ranc et al., 2008):

$$\dot{q}(T,f)=f\dot{Q}(T,f)\delta(x_1,x_2,x_3)=f\beta_{\mathrm{diff}}\dot{W}_p(T,f)\delta(x_1,x_2,x_3) \tag{1}$$

where $\dot{Q}$ is the heat intensity per cycle, $\dot{W}_p$ is the domain switching energy density per cycle, the fraction β_{diff} is the rate of domain switching energy converted into heat and remains nearly be 0.8 for PZT ceramics under purely electric loading (Chen et al., submitted for publication). δ is the Dirac function.

$$\delta(x_1,x_2,x_3)=\begin{cases}1(x_1,x_2,x_3)\in A_{\mathrm{DS}}(T,f)\\ 0(x_1,x_2,x_3)\notin A_{\mathrm{DS}}(T,f)\end{cases} \tag{2}$$

where A_{DS} is the reverse domain switching zone. It is noted that $\dot{W}_p$ and A_{DS} depend on both temperature *T* and frequency *f*.

Heat conductivity is governed by Fourier's law

$$\rho C\frac{\partial T}{\partial t}=\dot{q}(T,f)+k\Delta T \tag{3}$$

where ρ is the density of the ferroelectric ceramics, *C* is the heat capacity, *k* is the heat conductivity and Δ is the Laplacian operator.

The boundary conditions of heat losses due to the convection through the surface are given as

$$\left(\frac{\partial T}{\partial n}\right)_{x3=\pm\frac{d}{2}}+h(T-T_s)=0 \tag{4}$$

where $\partial/\partial n$ denotes differentiation in the direction of the outward normal to the surface, *h* is the surface heat transfer coefficient, T_s is the initial temperature throughout the plate and the ambient surroundings (air, oil, etc.), *d* is the thickness

of the sample.

In this paper, in order to predict the coupled fracture behavior, two quantitative relations need to be determined: (1) Determining geometry of the domain switching zone under alternative electric loading; (2) Modeling the self-heating induced mechanical fracture phenomenon.

The small scale switching (SSS) model (Yang and Zhu, 1998; Zhu and Yang, 1997, 1998) is an effective tool for the analysis of ferroelectric fracture mechanics. It is assumed that the switching zone size is considerably smaller than the specimen size. In this paper, however, the switching zone is comparable with the specimen size when the applied field is near or above the coercive field. Reverse large scale switching model (RLSS) for a central crack is needed.

As shown in Fig. 1, the ferroelectrics are consisted of ferroelectric tetragonal domains. The initial domain direction has an angle Φ with x_1 axis. The domain switching criterion was proposed based on the energy method (Hwang et al., 1995). If the electric word exceeds a threshold value, for an individual domain, the polarization direction may rotate by either 90° or 180°. If both directions meet Huang's criterion, the domain will rotate to the direction in which the work for switching maximizes, which is called the principle of domain switching choice. However, the energy barrier is temperature-dependent and frequency-dependent (Shin et al., 2007; Nelson et al., 2011). And a domain switching criteria is developed based on the experiments (Chen et al., submitted for publication)

$$E_i \Delta P_i(T,f) \geq 2E_c(T,f)P_s(T,f) = 2E_0P_0f_*^{a1+a3}T_*^{a2+a4} \tag{5}$$

in which

$$E_c(T,f) = 2E_{c0}f_*^{a_1}T_*^{a_2};\quad P_s(T,f) = P_0f_*^{a_3}T_*^{a_4};\quad f_* = \frac{f}{f_0};\quad T_* = \frac{T_c - T}{T_c - T_0} \tag{6}$$

where E_i represent the components of electric field vector, P_s is the spontaneous polarization, the right side $2P_sE_c$ denotes the temperature and frequency dependent energy barrier. f and T are the applied frequency and the ambient temperature, respectively. E_{c0} and P_0 is the coercive electric field and remnant polarization at the frequency f_0 and temperature T_0. T_c is the Curie temperature. a_1, a_2, a_3 and a_4 are the material constants and determined by the experimental data.

The components of polarization switching vector ΔP_i for 90° and 180° domain switching are expressed respectively:

For 90° domain switching

$$\Delta P_i = \sqrt{2}P_s\left[cos\left(\phi \pm \frac{3}{4}\pi\right);\quad \sin\left(\phi \pm \frac{3}{4}\pi\right)\right] \tag{7}$$

The plus and minus signs denote the anti-clockwise and clockwise domain switching respectively.

For 180° domain switching

$$\Delta P_i = -2P_s[\cos\phi;\ \sin\phi] \tag{8}$$

The remnant strain tensor is

$$\Delta\varepsilon_{ij} = \gamma_s\begin{bmatrix} -\cos 2\phi & -\sin 2\phi \\ -\sin 2\phi & \cos 2\phi \end{bmatrix} \tag{9}$$

Suppose an insulating central cracked ferroelectric body is loaded by a continuous alternative electric field E_2^∞. The full electric field solutions in the closed form are (Fang and Liu, 2013)

$$\boldsymbol{E} = E_2 + iE_1 = E_2^\infty\frac{\boldsymbol{z}}{\sqrt{\boldsymbol{z}^2 - a^2}} \tag{10}$$

where $\boldsymbol{z}=x_1+ix_2$ and $i=\sqrt{-1}$. The full electric field $\boldsymbol{E}$ will be reduced to two limiting cases: $\boldsymbol{E}\rightarrow E_2^\infty$ as $\boldsymbol{z}$ approaches infinite along the axis x_1. The square root singular electric field at the crack tip as $\boldsymbol{z}$ approaches $\pm a$ along the axis x_1.

Firstly, we consider the case when the direction of the first half-cycle electric field is same as the polarization one. In the first 1/4 cycle, the domain switching zone increases under higher electric field and reaches the maximum when $E=E_{max}$. There only exists the 90° domain switching in the rear crack, as shown in Fig. 7a. During the second 1/4 cycle, the electric field decreases from the minimum E_{max} to zero, and the shape of the domain switching remains unchanged. In the third 1/4 cycle, as shown in Fig. 7b, using the principle of domain switching choice in Eq.(5), zone I undergoes the reverse 180° domain switching, and new 180° domain switching occurs in zone III, while new 90° domain switching occurs in zone II. The shape of the new domain switching zone reaches its minimum when $E=E_{max}$. And the shape of the domain switching does not change in the fourth 1/4 cycle. In the next 1/4 cycle, zones I, II and III all undergo the reverse 180° domain switching.

Secondly, if the direction of the first half-cycle electric field is opposite to the polarization one. A similar procedure is used to obtain domain switching zone, as shown in Fig. 7c, d. It is interesting that the final reverse domain switching zone is same as that of the first case.

A reverse large scale switching (RLSS) model is developed to determine the reverse domain switching zone under alternative electric loading with the fixed frequency $f=1$ Hz and three different amplitude: $E=0.75$, 1.00, and $1.25E_c$. Based on the domain switching induced heat conclusion (Chen et al., 2013), the well-defined border of the reverse domain switching

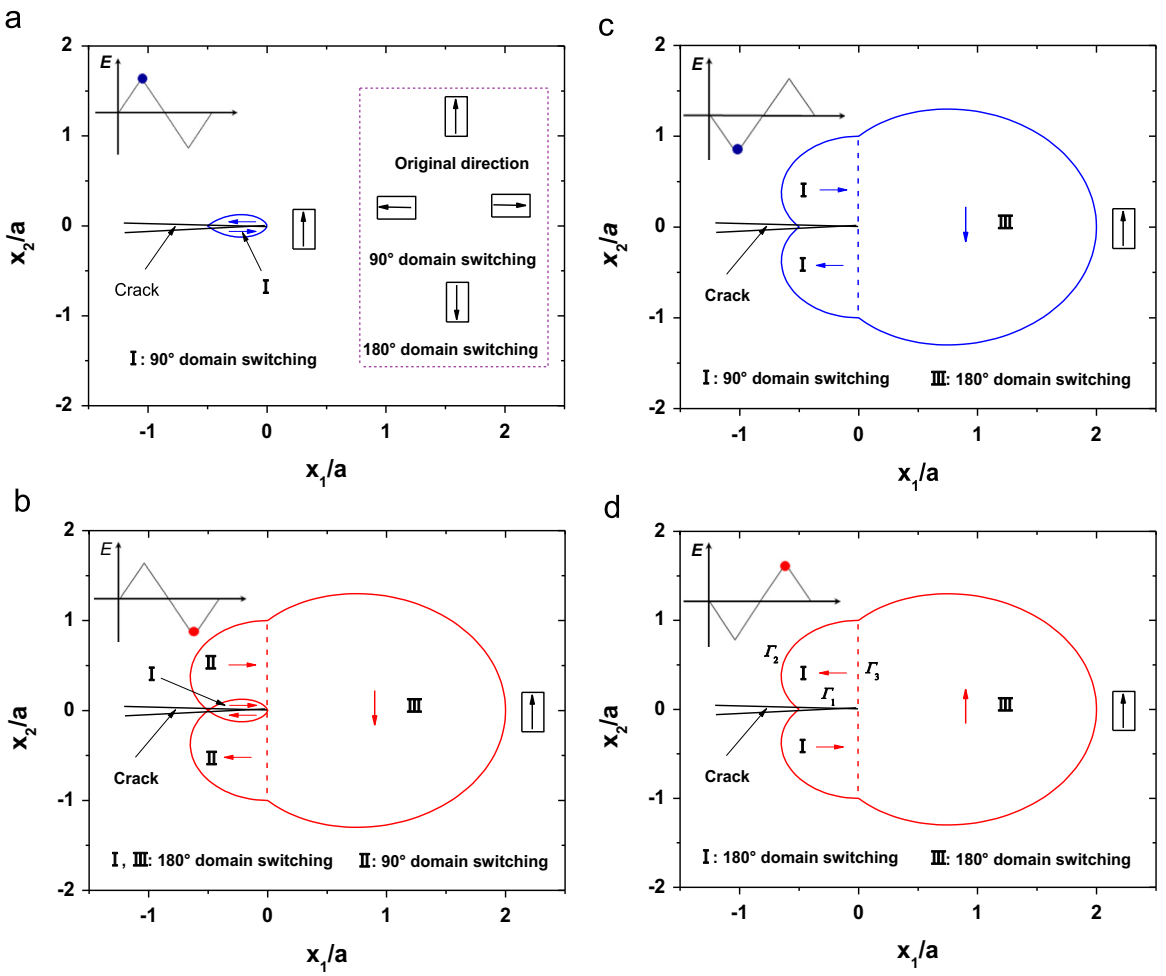

Fig. 7. Reverse domain switching at crack tip under alternative electric loading.

zone is determined experimentally based on the principle as follows: whether there are two temperature rise peaks in each cycle of the electric loading and the temperature rise is about 0.2 °C. For comparison, the results predicted by our RLSS model in this paper and Reverse Small Scale Switching (RSSS) model are all presented in Fig. 8a–c. It is found that the experimental data agrees well with those predicted by the RLSS model, while is much larger than those calculated by the RSSS model, which means that the RSSS model has the range of its application.

Based on the results of the reverse domain switching zone, we will solve the stress intensity factor (SIF) K_{tip}

$$K_{\text{tip}}(T) = K_{\text{app}} + \Delta K_{\text{ds}}(T) + \Delta K_{\text{tem}}(T) \tag{11}$$

where K_{app} represents the contribution from the piezoelectric effects under electric loading, which would be ignored here (Zhu and Yang, 1997); ΔK_{ds} represents the contribution from the electric-field-induced domain switching, which could be determined by the Eshelby–McMeeking–Evans method (Zhu and Yang, 1997). ΔK_{tem} represents the contribution from electric-field-induced thermal stresses by temperature gradient near the crack tip. According to the experimental data, there was a weaker temperature difference near and away the crack tip and on the order of 3 °C . Therefore, this effect was not considered in this paper.

Since the 180° domain switching produces little strain, contribution of the domain switching effects will be calculated along the 90° switching boundary. Following the same procedure

$$\Delta K_{\text{ds}} = \oint_{\Gamma_s} T_i h_i \, d\Gamma_i \tag{12}$$

where Γ_s is the whole 90° domain switching boundary of the reverse switching zone. It consisted of three segments Γ_1, Γ_2 and Γ_3 with the anti-clockwise direction, as shown in Fig. 8d. T_i represents the traction distribution acting along the boundary, h_i denotes the weight function.

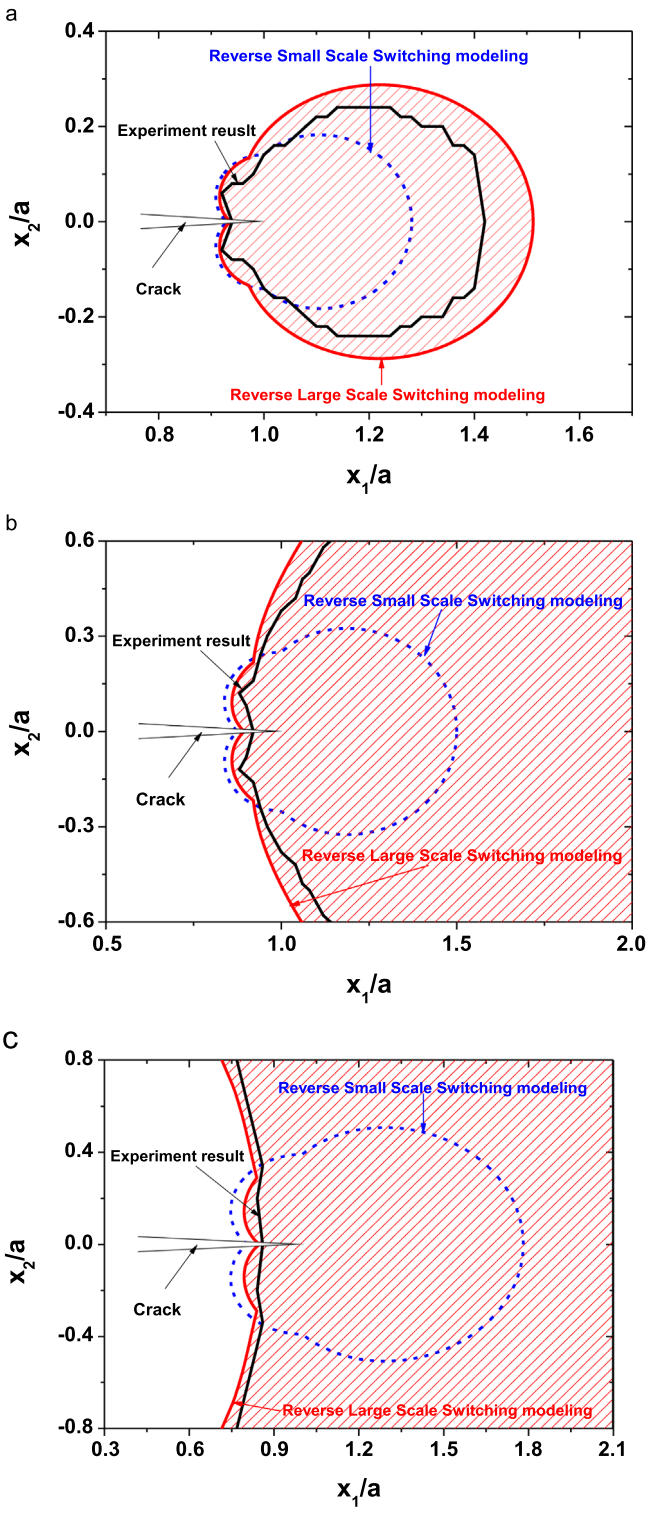

Fig. 8. (a)–(c) The switching zone predicted by the RSSS model, the RLSS model, and experimental result under three different driven electric field $E=0.75$, 1.00, and $1.25E_c$, respectively.

$$h_i(r,\varphi)=\frac{1}{(\hat{\kappa}+1)\sqrt{2\pi r}}\tilde{h}_i(\varphi) \tag{13}$$

where $\hat{\kappa}=3-4\gamma$ for the plane strain case while $\hat{\kappa}=(3-\gamma)/(1+\gamma)$ for the plane stress case, γ is the Poisson ratio, $\tilde{h}_i(\varphi)$ in the

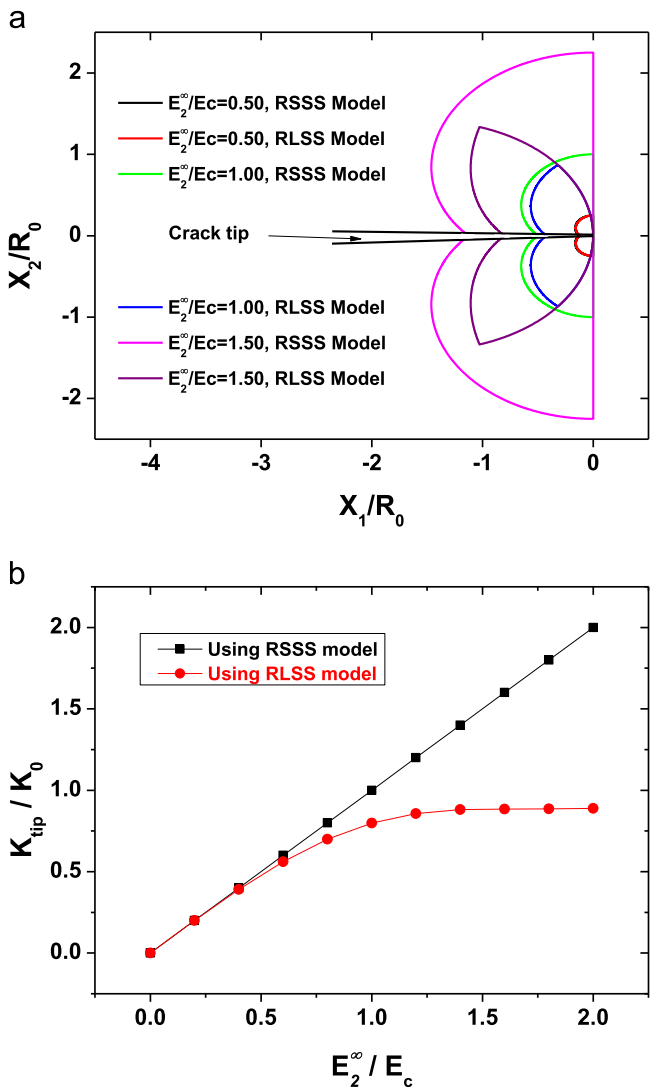

Fig. 9. The 90° switching boundary and dimensionless stress intensity factor V_s the dimensionless electric field using the SSS model and the LSS model. (a) 90° Switching boundary; and (b) dimensionless stress intensity factor.

polar representation $(r,\ \varphi)$.

$$\begin{Bmatrix} \tilde{h}_1(\varphi) \\ \tilde{h}_2(\varphi) \end{Bmatrix} = \begin{Bmatrix} (1-\hat{\kappa})\cos\dfrac{\varphi}{2} + \sin\varphi\,\sin\dfrac{3\varphi}{2} \\ (1+\hat{\kappa})\sin\dfrac{\varphi}{2} - \sin\varphi\,\cos\dfrac{3\varphi}{2} \end{Bmatrix} \tag{14}$$

and

$$T_i = \sigma_{ij}\, n_j = \frac{Y}{1+\gamma}\Delta\varepsilon_{ij}\, n_j \tag{15}$$

where Y denotes Young's modulus, n_j represents the outward normal of Γ_s.

Because the mismatched strain at the crack tip is caused mainly by the 90° domain switching, contribution of the domain switching effects will be calculated along the 90° switching boundary.

According to the SSS model proposed by Zhu and Yang (1998), the analytical solution for the 90° switching boundary of the SSS model is

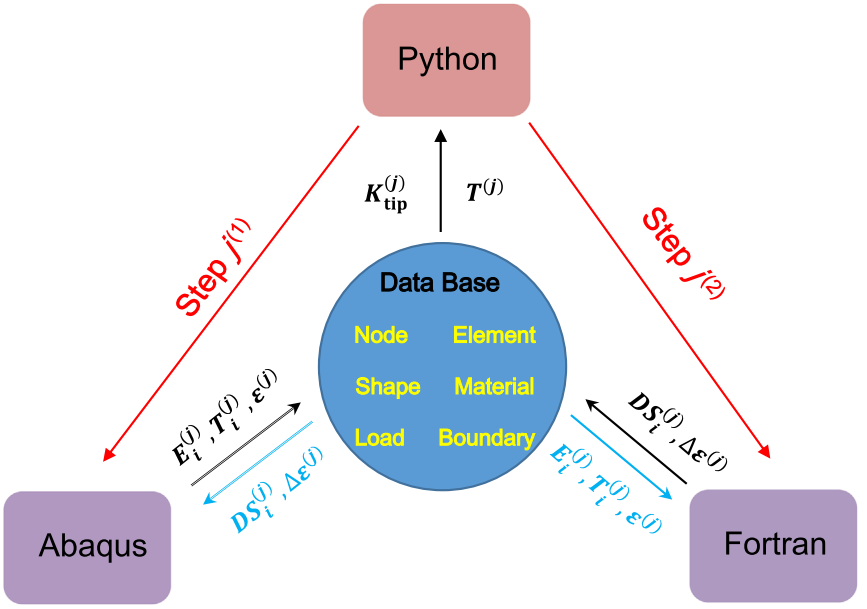

Fig. 10. Schematics of simulation implementation.

$$\sqrt{R} = -\sqrt{R_0}\frac{E_2^{\infty}}{E_c}\cos\left(\pm\frac{3}{4}\pi + \frac{\varphi}{2}\right) \tag{16}$$

where R is the polar radius, the plus and minus signs have the same meanings as those in Eq. (7), and $R_0 = a^2/4$.

As shown in Fig. 9, the boundary of LSS 90° domain switching and the dimensionless stress intensity factor are obtained numerically. For a clear comparison, the 90° domain switching zone for the RSSS and RLSS under different electric field amplitude are both presented, as shown in Fig. 9(a). With the increasing of the electric field, the shape of the 90° domain switching zone using the RSSS model remains the same, while that using the RLSS model changed dramatically. Under the electric loading of the level of one-half coercive field, difference between the size of domain switching zone calculated by the RSSS and that by the RLSS is negligible. However, the difference is much more pronounced when the electric field is approaching or exceeding the coercive field.

Fig. 9(b) presents the relation between the dimensionless stress intensity factor and the dimensionless electric field. Based on the model proposed by Zhu and Yang (1998), the net stress intensity factor for the RSSS case was obtained $K_{\text{tip}} = K_0\frac{E_2^{\infty}}{E_c}$, where $K_0 = \frac{9}{16\pi}\frac{Y_s\sqrt{\pi a}}{(1-\gamma^2)}$. The dimensionless SIF increases linearly with the ratio of the applied electric field to the coercive electric field. Compared with the results predicted by the RSSS model, the SIF for the case of the R LSS model needed to be calculated numerically. The dimensionless SIF has a linear relation with E/E_c at first, but increases nonlinearly from the point E/E_c=0.5. Therefore, the SIF using RSSS model has the range of its application when the applied electric field is lower than about 0.5 E_c. Furthermore, for both cases, the SIF increases with the decreasing of the coercive electric field. It means that with the temperature increase, the coercive electric field $E_c(T)$ decreases correspondingly, which leads to the increasing of stress intensity factor $K_{\text{tip}}(T)$.

Table 1
Material constants.

Name (Unit)		Value	Name (Unit)		Value
Elastic stiffness (× 10^{10} N/m^2)	c_{11}	12.60	**Fracture toughness (MPa m$^{1/2}$)**	K_{IC}	1
	c_{12}	5.50	**Heat conductivity (W/m/k)**	k	30
	c_{13}	5.30	**Heat capacity (J/kg/k)**	C	420
	c_{33}	11.70	**Convective coefficient (W/m^2/k)**	h	20
	c_{44}	3.53	**Remnant strain**	γ_s	0.003
Piezoelectric constants (× C/m^2)	e_{13}	−6.50	**Density (kg/m^3)**	ρ	7.5 × 10^3
	e_{33}	23.30	**Dielectric**	κ_{11}	151
	e_{15}	17.00	**constants (× 10^{-10} C/Vm)**	κ_{33}	130

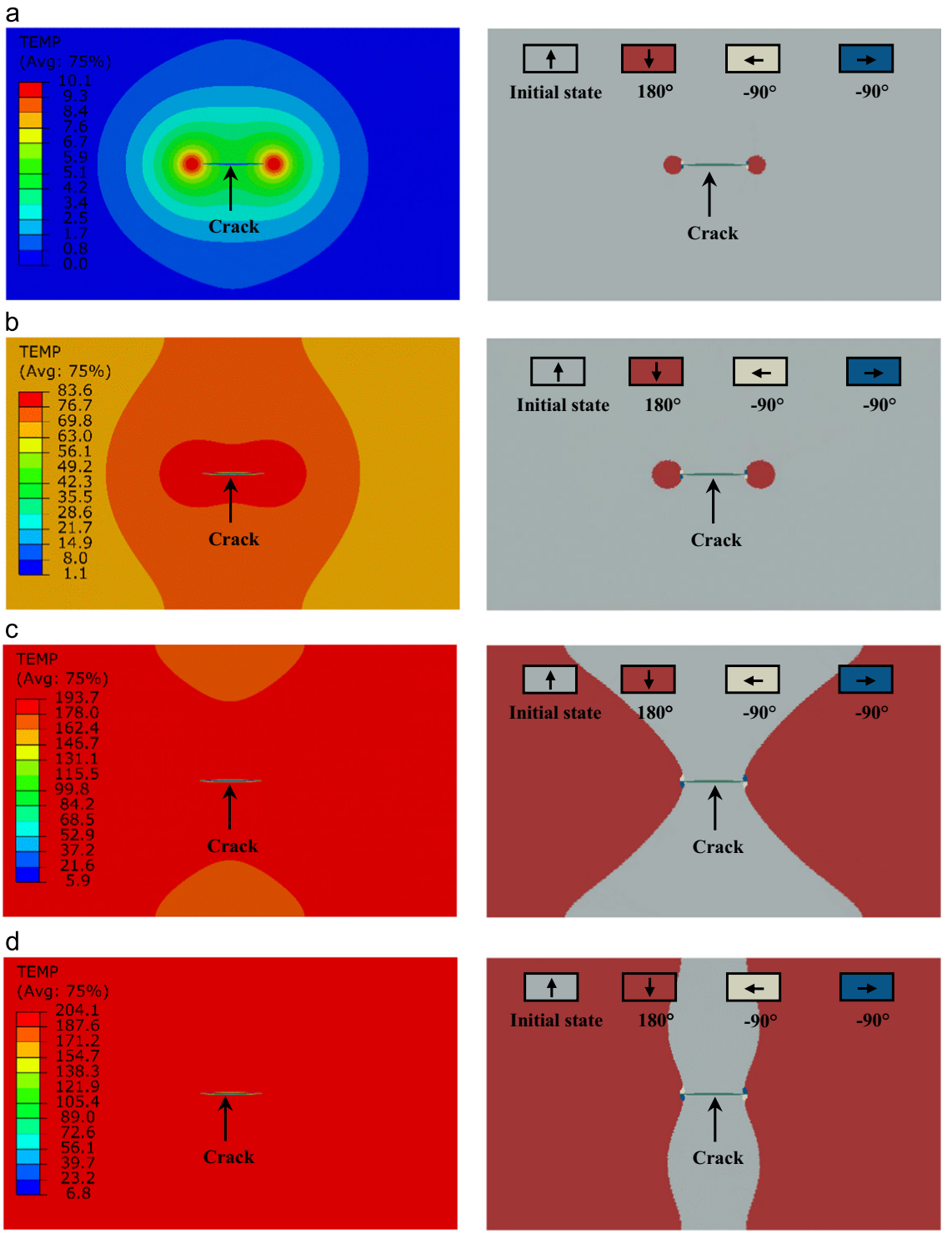

Fig. 11. Numerical simulation of temperature rise field and domain switching zone in the specimen with cycles, $f=1$ kHz, $E=0.75\,E_{c0}$, see Supplementary Movie 3. (a) 0.01×10^4 cycle, (b) 5×10^4 cycle, (c) 9.46×10^4 cycle and (d) 10×10^4 cycle.

3.2. *Finite-element simulations*

Finite element method (FEM) is useful and convenient to solve the ferroelectric problem, especially in adopting the nonlinear constitutive relations and simulating the field distribution in ferroelectric structures. At present, both the home-

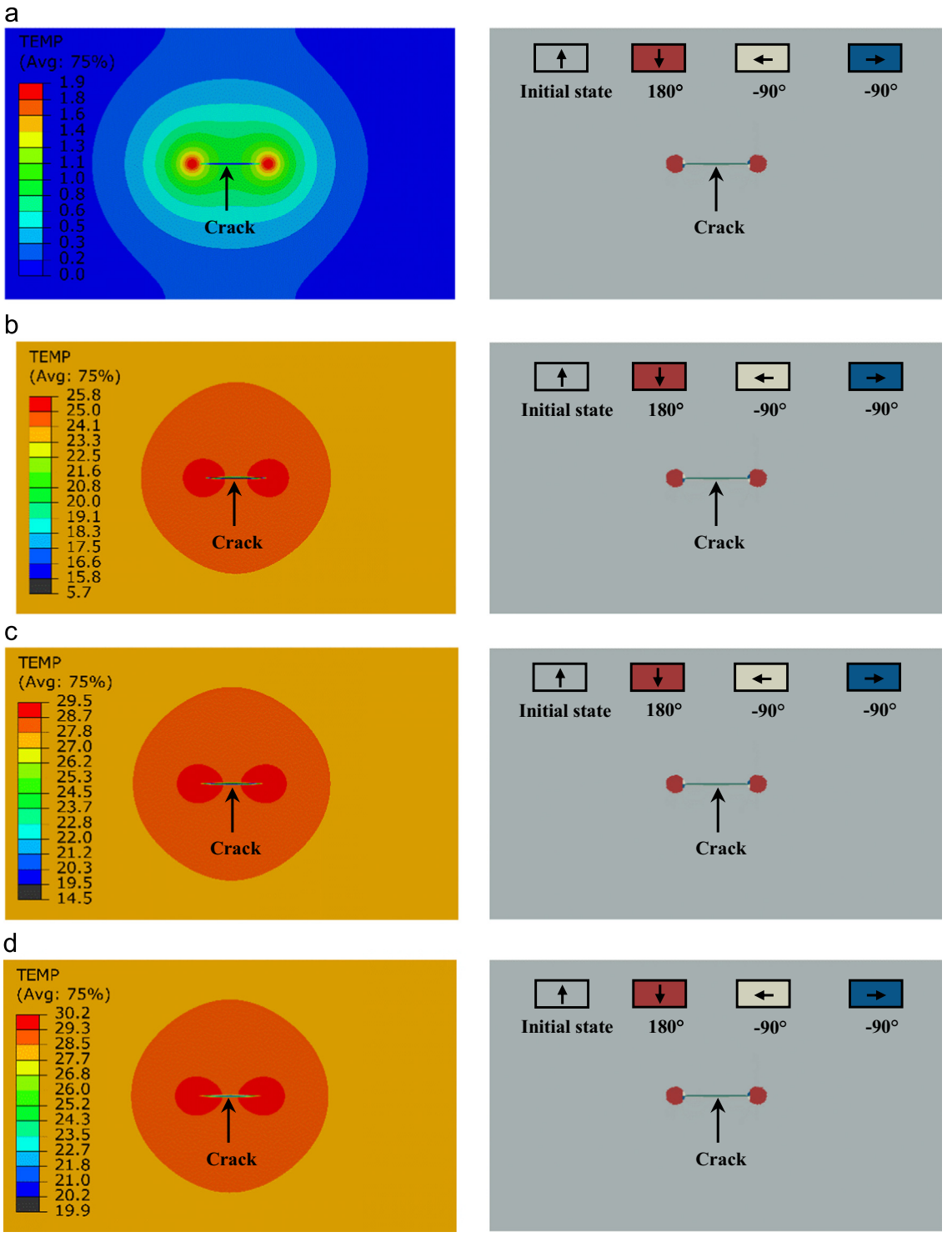

Fig. 12. Numerical simulation of temperature rise field and domain switching zone in the specimen with cycles, $f=100$ Hz, $E=0.75E_{c0}$, see Supplementary Movie 6. (a) 0.01×10^4 cycle, (b) 2×10^4 cycle, (c) 4×10^4 cycle, and (d) 6×10^4 cycle.
Supplementary material related to this article can be found online at doi:10.1016/j.jmps.2015.04.014zone.

made finite element model and the commercial software such as Abaqus cannot deal with the coupling between the ferroelectric domain switching and the heat conduction (Fang et al., 2013). In our work a coupled electro-thermal-mechanical finite element model is established and implemented into ABAQUS using the ABAQUS Scripting Interface (ASI) and Python language which could efficiently deal with the pre- and post-processing tasks of ABAQUS.

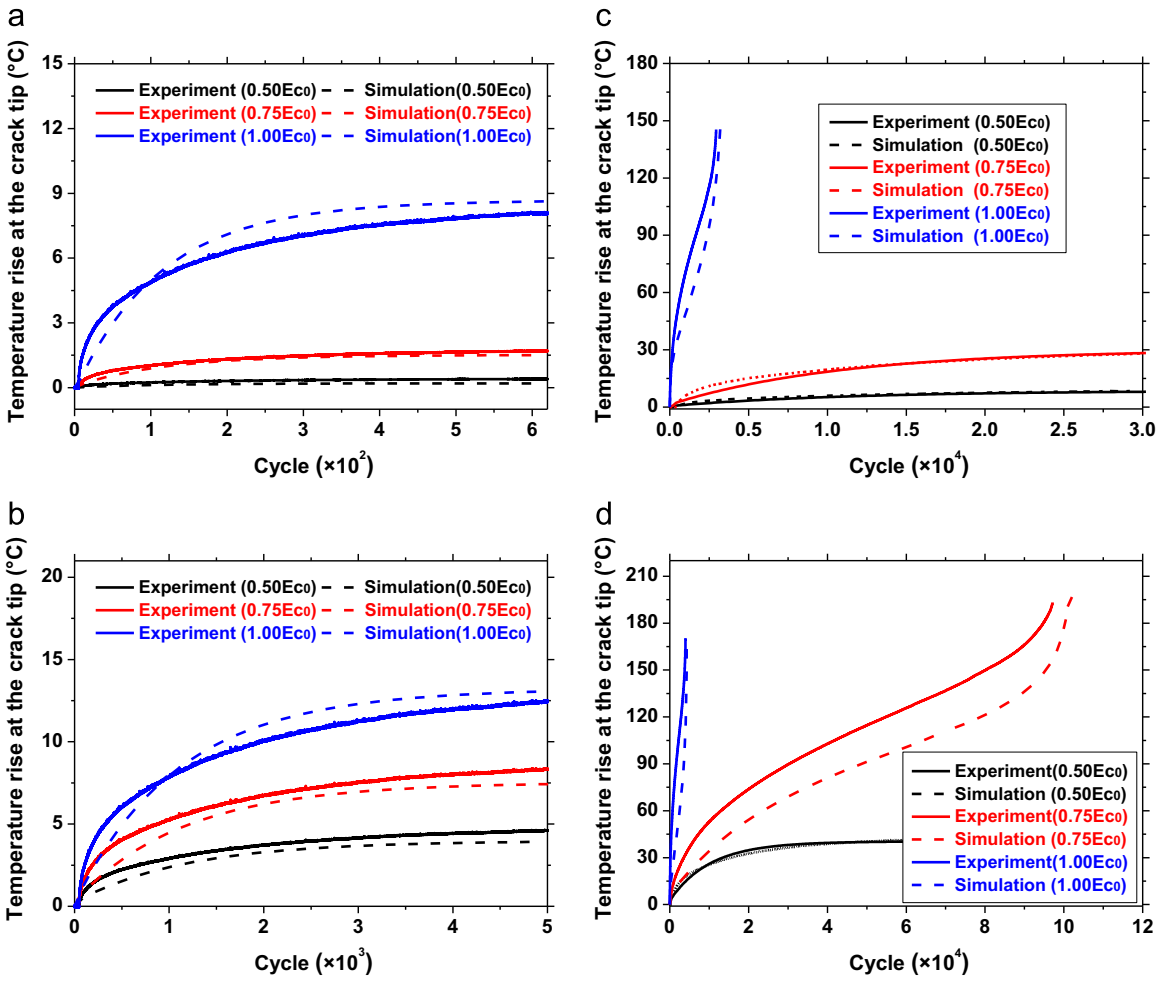

Fig. 13. Comparing between the FEA method and experiment. (a) $f=1$ Hz, (b) $f=10$ Hz, (c) $f=100$ Hz and (d) $f=1$ *k*Hz.

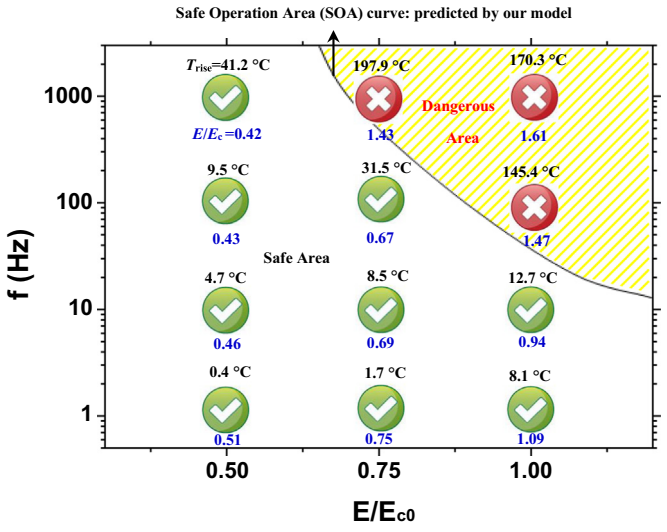

Fig. 14. Fracture phase diagram and the SOA curve with respect to different amplitude and frequency.

The simulation frame composes of four parts, as shown in Fig. 10. (1) Python Part. It controls the entire computational process. The code based on the Python language includes the Abaqus model description and the termination criterion for iteration. It submits the input file to be solved by the Abaqus Part, stores the Abaqus output-data to the Data base part, and then executes the Fortran Part with the new data. This procedure controlled by the Python is repeated until the termination condition is fulfilled. And a convergent temperature and domain switching distribution will be obtained finally. (2) Abaqus Part. In each iteration, with the updated heat source conditions, this part is to solve the electric field $E_i^{(j)}$, the temperature field $T_i^{(j)}$ and the strain field $\varepsilon^{(j)}$ from the given input files. (3) Fortran part. This part uses the electric and temperature field to update the domain direction of each element with the temperature and frequency dependent domain switching criteria. Then the reverse domain switching area $DS_i^{(j)}$, the intensity of the heat source and the remnant strain field $\Delta\varepsilon^{(j)}$ are updated. (4) Data Base Part. It provides a place to store the Abaqus output-data and the Fortran results.

A 3D FE model was constructed using the Abaqus Part. The geometric parameters were the same as that of the experimental specimen. The triangular elements C3D6E were used in this simulation, and the mesh was refined near the crack tip. The impermeable electric boundary condition along the crack was adopted. The poling direction was perpendicular to the crack, namely $\Phi = 90°$. The basic formulas of electric-mechanical FEM simulating the nonlinear behavior of the ferroelectric material was developed in our early work and would not be covered again (Zhao et al., 2010). The material constants are listed in Table 1. The material constants in Eq. (5) were determined by experiments, $a_1=0.013$, $a_2=0.613$, $a_3=-0.107$ and $a_4=0.263$.

Using the proposed nonlinear FEA method, simulations were carried out firstly for two loading cases: $f=1$ *k*Hz, $E=0.75$ E_{c0}; $f=100$ Hz, $E=0.75$ E_{c0}. Figs. 11 and 12 show the simulation results of the temperature field and the domain switching distribution in the specimen at various times. For the loading condition of $f=1$ *k*Hz, $E=0.75E_{c0}$, before the reverse inflection point, reverse domain switching and heat generation occur only at the crack tip, as show in Fig. 11(a) and (b). After the reverse inflection point, reverse domain switching and rapid temperature change happen in the whole bulk except the zone behind the crack tip, as show in Fig. 11(c) and (d). However, as show in Fig. 12(a) and (b), when the samples are under cyclic alternative electric loading at low frequency ($f=100$ Hz) and the same amplitude, reverse domain switching zone and temperature quickly reach a stable state.

Fig. 13 gives the comparison of the temperature evolution at the crack tip between the simulation and experiment. It can be seen that the FEA predicts correctly the shape of the temperature evolution curve for all the 12 cases. Two types of samples exhibiting different temperature rise behavior are observed. Three among the twelve samples, ($f=0.1$ *k*Hz, $E=E_{c0}$; $f=1$ *k*Hz, $E=0.75E_{c0}$; $f=1$ *k*Hz, $E=1E_{c0}$), show the same temperature change tendency. We see that rapid temperature increase and instability occur in these samples, as shown in Fig.13 (c) and (d). The FEA method successfully simulates the "*S*" shape of the temperature evolution curve at the crack tip. Before the reverse inflection point, temperature rises moderately induced only by the domain switching around the crack tip, while temperature changes quickly caused by the domain switching of nearly the whole bulk. In contrast, temperature in the rest nine samples remain stable. The temperature becomes finally balanced at the crack tip and the crack does not propagate, as shown in Fig. 13(a)–(d). The simulation temperature rises quickly and reaches a stable value, which resembles the experimental phenomena.

3.3. Fracture phase map

After being validated by the experimental results, this model further predicts the self-heating induced crack under electric loading with different frequency and amplitude. The fracture phase diagram to show the SOA curve as a function of both the frequency and the amplitude of an electric field is obtained in Fig. 14. It tells the boundary that whether a crack in PZT materials subjected to an alternative electric field with a combination of frequency and magnitude is within safe operation or not. For frequency and magnitude falling in the domain above this boundary, the temperature at the crack tip continues to rise uncontrolledly until the fracture occurs. While below the SOA curve, switching domain induced temperature rise will increase mildly and approach an equilibrium state. The crack remains stable without prolongation.

4. Conclusions

We report a novel experimental setup that enables us to observe the domain switching zone of ferroelectrics at the crack tip and self-heating induced crack propagation *in-situ*. Based on our experiments, we observe two distinct phenomena: (a) temperature in the crack tip increases in an unstable and uncontrolled way when samples are subjected to alternative electric loading at high frequency or large amplitude, and (b) temperature rise quickly saturates and no crack growth is observed when loading with low frequency or small amplitude. We propose a theoretical model to predict the reverse domain switching zone, which agrees well with the experimental results. A fracture phase diagraph is obtained by combining our theoretical results and experimental observations, which provides guidance to design the piezoelectric/ferroelectric devices.

Acknowledgment

We are grateful for the support by National Natural Science Foundation of China under Grants #11302260, #11090330, #11090331, #11072003 and #11272222. Support by the National Basic Research Program of China (#G2010CB832701) is also acknowledged.

References

Abdollahi, A., Arias, I., 2012. Phase-field modeling of crack propagation in piezoelectric and ferroelectric materials with different electromechanical crack conditions. J. Mech. Phys. Solids 12 (60), 2100–2126.
Abdollahi, A., Arias, I., 2013. Conducting crack propagation driven by electric fields in ferroelectric ceramics. Acta Mater. 19 (61), 7087–7097.
Abdollahi, A., Arias, I., 2014. Three-dimensional simulation of crack propagation in ferroelectric polycrystals: effect of combined toughening mechanisms. Acta Mater. 65, 106–117.
Beom, H.G., Jeong, K.M., 2005. Crack growth in ferroelectric ceramics under electric loading. Acta Mech. 1–4 (177), 43–60.
Cao, H., Evans, A.G., 1994. Electric-field-induced fatigue crack growth in piezoelectrics. J. Am. Ceram. Soc. 7 (77), 1783–1786.
Cao, H.C., Evans, A.G., 1994. Electric-field-induced fatigue-crack growth in piezoelectrics. J. Am. Ceram. Soc. 7 (77), 1783–1786.
Chen, H., Pei, Y., Liu, B., Fang, D., 2013. Rate dependant heat generation in single cycle of domain switching of lead zirconate titanate via in-situ spontaneous temperature measurement. Appl. Phys. Lett. 24 (102), 242912.
Chen, H., Wang, H., Pei, Y., Liu, B., Fang, D., 2015. Self-heating induced breakdown of ferroelectric solids, (submitted for publication).
Eerenstein, W., Mathur, N.D., Scott, J.F., 2006. Multiferroic and magnetoelectric materials. Nature 7104 (442), 759–765.
Fang, D., Liu, B., Sun, C.T., 2004. Fatigue crack growth in ferroelectric ceramics driven by alternating electric fields. J. Am. Ceram. Soc. 5 (87), 840–846.
Fang, D., Liu, J., 2013. In: Fracture Mechanics of Piezoelectric and Ferroelectric SolidsSpringer, Berlin.
Fang, D., Zhang, Y., Mao, G., 2011. A COD fracture model of ferroelectric ceramics with applications in electric field induced fatigue crack growth. Int. J. Fract. 2 (167), 211–220.
Fang, D.N., Li, F.X., Liu, B., Zhang, Y.H., Hong, J.W., Guo, X.H., 2013. Advances in developing electromechanically coupled computational methods for piezoelectrics/ferroelectrics at multiscale. Appl. Mech. Rev. 6 (65), 60802.
Fang, F., Yang, W., Zhang, F.C., Luo, H.S., 2005. Fatigue crack growth for $BaTiO_3$ ferroelectric single crystals under cyclic electric loading. J. Am. Ceram. Soc. 9 (88), 2491–2497.
Fang, F., Yang, W., Zhang, F.C., Qing, H., 2007. Domain structure evolution and fatigue cracking of $<001>$ oriented $[Pb(Mg_{1/3}Nb_{2/3})O_3]_{0.67}(PbTiO_3)_{0.33}$ ferroelectric single crystals under cyclic electric loading. Appl. Phys. Lett. 8 (91).
Fang, F., Yang, W., Zhang, F.C., Qing, H., 2008. In-situ observation of fatigue crack growth for $<001>$-oriented rhombohedral $Pb(Mg_{1/3}Nb_{2/3})O_3$-$PbTiO_3$ ferroelectric single crystal. Int. J. Fract. 2 (151), 161–168.
Gehrig, F., Jelitto, H., Schneider, G.A., 2008. Fracture criterion for a conducting crack in poled PZT-PIC 151 investigated by stable crack growth. Acta Mater. 2 (56), 222–229.
Haertling, G.H., 1999. Ferroelectric ceramics: history and technology. J. Am. Ceram. Soc. 4 (82), 797–818.
Härdtl, K.H., 1982. Electrical and mechanical losses in ferroelectric ceramics. Ceram. Int. 4 (8), 121–127.
Hwang, S.C., Lynch, C.S., Mcmeeking, R.M., 1995. Ferroelectric/ferroelastic interactions and a polarization switching model. Acta Mater. 5 (43), 2073–2084.
Jeong, K.M., Beom, H.G., 2004. Conducting crack growth in ferroelectric ceramics subjected to electric loading. Smart Mater. Struct. 2 (13), 275–282.
Jiang, B., Bai, Y., Li, M.C., Mwenya, T., 2014. In situ observation of correlations between domain switching and crack propagation in $BaTiO_3$ single crystals under coupling of mechanical and electric loads. Scr. Mater. 70, 47–50.
Jiehui, Z., Takahashi, S., Yoshikawa, S., Uchino, K., de Vries, J.W.C., 1996. Heat generation in multilayer piezoelectric actuators. J. Am. Ceram. Soc. 12 (79), 3193–3198.
Kuna, M., 2010. Fracture mechanics of piezoelectric materials—where are we right now? Eng. Fract. Mech. 2 (77), 309–326.
Liu, B., Fang, D.N., Hwang, K.C., 2002. Electric-field-induced fatigue crack growth in ferroelectric ceramics. Mater. Lett. 5 (54), 442–446.
Livne, A., Bouchbinder, E., Svetlizky, I., Fineberg, J., 2010. The near-tip fields of fast cracks. Science 5971 (327), 1359–1363.
Lynch, C.S., Chen, L., Suo, Z., Mcmeeking, R.M., Yang, W., 1995. Crack-growth in ferroelectric ceramics driven by cyclic polarization switching. J. Intell. Mater. Syst. Struct. 2 (6), 191–198.
Lynch, C.S., Yang, W., Collier, L., Suo, Z., Mcmeeking, R.M., 1995. Electric field induced cracking in ferroelectric ceramics. Ferroelectrics 1–4 (166), 11–30.
Nelson, C.T., Gao, P., Jokisaari, J.R., Heikes, C., Adamo, C., Melville, A., Baek, S., Folkman, C.M., Winchester, B., Gu, Y., 2011. Domain dynamics during ferroelectric switching. Science 6058 (334), 968–971.
Ranc, N., Wagner, D., Paris, P.C., 2008. Study of thermal effects associated with crack propagation during very high cycle fatigue tests. Acta Mater. 15 (56), 4012–4021.
Scott, J.F., 2007. Applications of modern ferroelectrics. Science 5814 (315), 954–959.
Shin, Y., Grinberg, I., Chen, I., Rappe, A.M., 2007. Nucleation and growth mechanism of ferroelectric domain-wall motion. Nature 7164 (449), 881–884.
Soh, A.K., Lee, K.L., Fang, D.N., 2003. On the effects of an electric field on the fracture toughness of poled piezoelectric ceramics. Mater. Sci. Eng. A: Struct. 1–2 (360), 306–314.
Stewart, M., Cain, M.G., 2014. In: Measurement and Modelling of Self-heating in Piezoelectric Materials and DevicesSpringer, Netherlands.
Uchino, K., 1998. Materials issues in design and performance of piezoelectric actuators: an overview. Acta Mater. 11 (46), 3745–3753.
Weitzing, H., Schneider, G.A., Steffens, J., Hammer, M., Hoffmann, M.J., 1999. Cyclic fatigue due to electric loading in ferroelectric ceramics. J. Eur. Ceram. Soc. 6 (19), 1333–1337.
Westram, I., Kungl, H., Hoffmann, M.J., Rodel, J., 2009. Influence of crystal structure on crack propagation under cyclic electric loading in lead–zirconate–titanate. J. Eur. Ceram. Soc. 3 (29), 425–430.
Westram, I., Oates, W.S., Lupascu, D.C., Rödel, J., Lynch, C.S., 2007. Mechanism of electric fatigue crack growth in lead zirconate titanate. Acta Mater. 1 (55), 301–312.
Westram, I., Ricoeur, A., Emrich, A., Rodel, J., Kuna, M., 2007. Fatigue crack growth law for ferroelectrics under cyclic electrical and combined electro-mechanical loading. J. Eur. Ceram. Soc. 6 (27), 2485–2494.
Yang, W., Zhu, T., 1998. Switch-toughening of ferroelectrics subjected to electric fields. J. Mech. Phys. Solids 2 (46), 291–311.
Zhang, Y.H., Li, J.Y., Fang, D.N., 2013. Fracture analysis of ferroelectric single crystals: domain switching near crack tip and electric field induced crack propagation. J. Mech. Phys. Solids 1 (61), 114–130.
Zhao, X.J., Liu, B., Fang, D.N., 2010. Study on electroelastic field concentration around the electrode tip in multilayer ferroelectric actuators of two designs and their optimizations. Int. J. Plasticity 4 (26), 533–548.
Zhu, T., Yang, W., 1997. Toughness variation of ferroelectrics by polarization switch under non-uniform electric field. Acta Mater. 11 (45), 4695–4702.
Zhu, T., Yang, W., 1998. Fatigue crack growth in ferroelectrics driven by cyclic electric loading. J. Mech. Phys. Solids 1 (47), 81–97.